PAPER

Check for updates

Triple-shape memory, magneto-response, and piezo-resistive flexible composites: multiple-sensing and switchable actuating†

Tao Hu,[a] Shouhu Xuan, ✶[a] Quan Shu,[a] Zhenbang Xu,[b] Longjiang Shen,[c] Jun Li[d] and Xinglong Gong ✶[a]

Flexible strain sensors made of conductive composites provide an opportunity for monitoring human motions and external stimuli. However, it is still in pursuit to fabricate multifunctional strain sensors with shape memory effects to further broaden the practical applications. Herein, we designed and fabricated a high-temperature liquid metal–based magneto-resistive strain sensor with a triple-shape memory effect, stimulus-dependent conductivity, and magnetically driven property. The shape memory effect endowed the sensor with the ability to adapt its morphology to detect and fix on the objects with an arbitrary shape. The stimulus-dependent conductivity caused the sensor to generate a corresponding electrical signal when it detected any human motion and magnetic field. The magnetically driven properties broadened the application of the sensor, such as a smart gripper. Therefore, this multifunctional flexible strain sensor could be a good candidate for future intelligent electronics such as e-skins, soft robotics, morphing structures, and biomedical devices.

Introduction

Recently, with the rapid development of flexible electronics such as flexible sensors, e-skins, smart wearable devices, and soft robotics, there was an increasing awareness of the flexible strain sensors.[1–12] To achieve conductive and flexible features in these sensors, effective methods for integrating a conductive filler and an insulating polymer matrix together became essential. Some conductive composite sensors consisted of a laminated conductive layer and a stretchable substrate layer such as conductive films and networks, complicated conductive patterns, and rigid electronic components integrated on a soft substrate. Besides, many conductive composites were fabricated by directly mixing conductive fillers such as carbon nanotubes,[5,13,14] graphenes,[2,15–17] metal microparticles and nanowires[11,18,19] into a polymeric matrix. Recently, liquid metal (LM) was utilized as a liquid-phase conductive filler due to its high electrical and thermal conductivity, arbitrary shape reconfigurability, negligible toxicity, controllable melting point, and healing capability.[3,9,17,20–34] After being dispersed into the matrix, the liquid metal would break into microdroplets, which could deform with the matrix and retain the properties. However, the LM-embedded composites were often insulating, but became conductive once the LM microdroplets ruptured and contacted with others, which made these composite sensors exhibit little response to external strain. The single functionality further confined the development of LM-embedded composite sensors. To improve the responsive capability and broaden the practical application, there was a strong need for more facile and effective approaches to develop highly sensitive LM-embedded conductive composite sensors consisting of LM and other multifunctional materials.

Shape memory polymers (SMPs) are a kind of temperature-sensitive material for which could be fixed into a programmed temporary shape and then recover the original shape under external heat, light and chemical environment.[35–40] The crystallization/melting point T_m of the temperature-controlling component determined the shape memory effect of a temperature-triggered SMP. During a shape memory cycle, SMP was programmed into a temporary shape at a temperature higher than T_m. After cooling

[a] CAS Key Laboratory of Mechanical Behavior and Design of Materials, Department of Modern Mechanics, CAS Center for Excellence in Complex System Mechanics, University of Science and Technology of China, Hefei 230027, P. R. China. E-mail: gongxl@ustc.edu.cn, xuansh@ustc.edu.cn

[b] CAS Key Laboratory of On-orbit Manufacturing and Integration for Space Optics System, Changchun Institute of Optics, Fine Mechanics and Physics, Chinese Academy of Sciences, Changchun 130033, Jilin, China

[c] Hunan Bogie Engineering Research Center, Zhuzhou 412000, Hunan, China

[d] Anhui Weiwei Rubber Parts Group Co. Ltd, Tongcheng 231400, Anhui, China

† Electronic supplementary information (ESI) available: The compressive stress and the resistance changes *versus* compressive strain in loading and unloading phases of PPLC sensor. Representative tensile stress *versus* tensile strain curves of the PPLC specimen and damaged PPLC specimen. The corresponding temperature variation along the centerline of PPLC sensor during the real-time monitoring process. See DOI: 10.1039/d1tc01060c

6568 | *J. Mater. Chem. C*, 2021, **9**, 6568–6578

This journal is © The Royal Society of Chemistry 2021

and unloading the stimuli, SMP would recover its original shape when heated at a temperature higher than T_m again. Because multifunctional flexible strain sensors were often employed to detect objects with a complex morphology, SMP could meet the requirement of multiple shape manipulations well, such as attaching, detecting and fixing on the objects. However, the traditional SMP showed the drawback of only one-way shape memory actuation and single functionality. To further expand its applications in multifunctional flexible strain sensors, the hybrid composites with more functionalities and reprogrammable shape memory effects consisting of SMPs and other multifunctional materials need to be developed.

Moreover, among the multifunctional materials, the magneto-sensitive materials (MSM) consisting of magnetic particles and a non-magnetic polymeric matrix also have aroused great interest thanks to the untethered control for deformation, switchable mechanical properties, and non-contact sensing behavior. The interactions among the magnetic particles made them aggregate along the magnetic field, and then the mechanical properties of MSM were significantly enhanced. Owing to the special magnetic-induced properties, flexible sensors[23,24,32,41–43] and actuators[37,44–47] based on MSM were developed by the combination of conductive fillers, magnetic particles, and polymeric matrix. With the loading and unloading of magnetic field, effective conductive pathways in these sensors would be broken and reformed by magnetic particles, which led to the variation in conductivity. The magnetic force of these particles also endowed MSM with the magnetically driven property, to achieve the untethered control for deformation. To this end, according to the high electrical/thermal conductivity and controllable melting point of LMs, temperature-dependent properties of SMPs, the soft nature and magneto-sensitivity/drivability of MSMs, the integration of LMs, SMPs and MSM would be advantageous for developing multifunctional flexible strain sensors with high sensing performance, multiple sensitivity and extensive prospects.

In this work, a high-temperature liquid metal (HLM)-based magneto-resistive strain sensor (PPLC sensor) with the advantages of simple fabrication, triple-shape memory effect, stimulus-dependent conductivity, good magnetically driven property was developed. The PPLC sensor was fabricated by directly dispersing the HLM particles and carbonyl iron particles (CIPs) in the polyurethane (PU)–polycaprolactone (PCL) matrix. In this multifunctional composite sensor, the HLM particles and CIPs could form effective conductive pathways, which could be selectively controlled by adjusting the compressive strain and magnetic flux density. In addition, temperature-controlling components HLM and PCL could be crystallized/melted in the sensor at different temperatures. Thus, the sensor realized triple-shape memory effects with good repeatability, which could be integrated with an electromagnetic device to measure the changes in the magnetic field and heat. A possible mechanism was proposed to analyze the sensing performance. Finally, a smart alarm system and a six-arm smart gripper were constructed from the PPLC sensor. The multiple sensing and switchable actuating further demonstrated its wide potential for multifunctional flexible electronics.

Experimental section

Materials and preparation

First, the low crosslinking PU was self-prepared and the method has been reported in our previous work.[43] Then the PCL pellets (Zhanyang Polymer Material Co., Ltd China) were melted and fully mixed with PU (weight ratio 2 : 8) at 80 °C. Afterward, the HLM (44.7 wt% Bi, 22.6 wt% Pb, 19.1 wt% In, 8.3 wt% Sn and 5.3 wt% Cd, density 9.36 g cm^{-3}, Yongcheng Metal Material Co., Ltd China) and CIPs (type CN, BASF) were added to the matrix. The HLM was fully stirred in the PU–PCL matrix until no obvious HLM precipitation could be found in the beaker. Here, the weight fraction of PU–PCL was kept at 10 wt%, and the content of the HLM in PPLC varied from 80 wt% to 40 wt%, while the weight fraction of CIPs varied from 10 wt% to 50 wt%. The mixture was stirred at 80 °C for 1 h to homogenously separate the HLM and iron particles inside. Finally, the mixture was compressed into a mold and pre-structured at 80 °C for 30 min, and then 1 T magnetic field was generated using a magnetic power system (IGLF-150, Beijing Saidi New Electromechanical Technology Co., China) (Fig. 1a). Poly-dimethylsiloxane (PDMS, Sylard 184, curing ratio 10 : 1) cured in a 3D-printed mold was used as a shell to encapsulate PPLC.

The as-made PPLC exhibited temperature-dependent properties due to the different melting points of PCL (T_{pcl} = 58 °C) and HLM (T_{lm} = 47 °C). The PPLC sensor was stiff enough to support the permanent magnet and maintain its shape at room temperature (25 °C). After heating for several minutes, the temperature of PPLC reached 58 °C, thus the PCL crystals were melted, and the PPLC sensor was dramatically softened which could not support the magnet and maintain the shape anymore. Finally, the magnet sank into PPLC, which must be owing to the softening and magnetic properties of PPLC (Fig. 1b and c, Movie S1, ESI†). The PPLC sensor also possessed good flexibility under various mechanical stimuli like bending and compressing (Fig. 1d and f).

In Fig. 1g, the neat surface of PU–PCL proved that the PCL pellets were totally melted and successfully mixed with PU without any residual component. Then, the CIPs were embedded in the PU–PCL matrix and aligned in chains along the applied magnetic field in PU–PCL–CI (Fig. 1h). Furthermore, the white sphere particles embedded in the matrix demonstrated that the added HLM was broken into particles with a diameter of micrometers (Fig. 1i). The EDS elemental mappings further proved that the CIPs and HLM particles were mostly in spherical morphologies and well dispersed in the matrix (Fig. 1j). The PPLC sensor with CIPs, HLM particles, and PU–PCL matrix was fabricated, which was a new approach of the multifunctional flexible strain sensor.

Characterization

The morphology of PPLC was characterized using a scanning electron microscope (SEM, Gemini 500, Carl Zeiss Jena Germany), and the digital and thermal images were acquired using a digital camera (D1700, Nikon) and a thermal camera (ImageIR 8300, InfraTec Germany). Hysteresis Measurement of Soft and Hard Magnetic Materials (HyMDC Metis, Leuven, Belgium) and a commercial rheometer (Physica MCR 302, Anton Paar Co., Austria)

This journal is © The Royal Society of Chemistry 2021

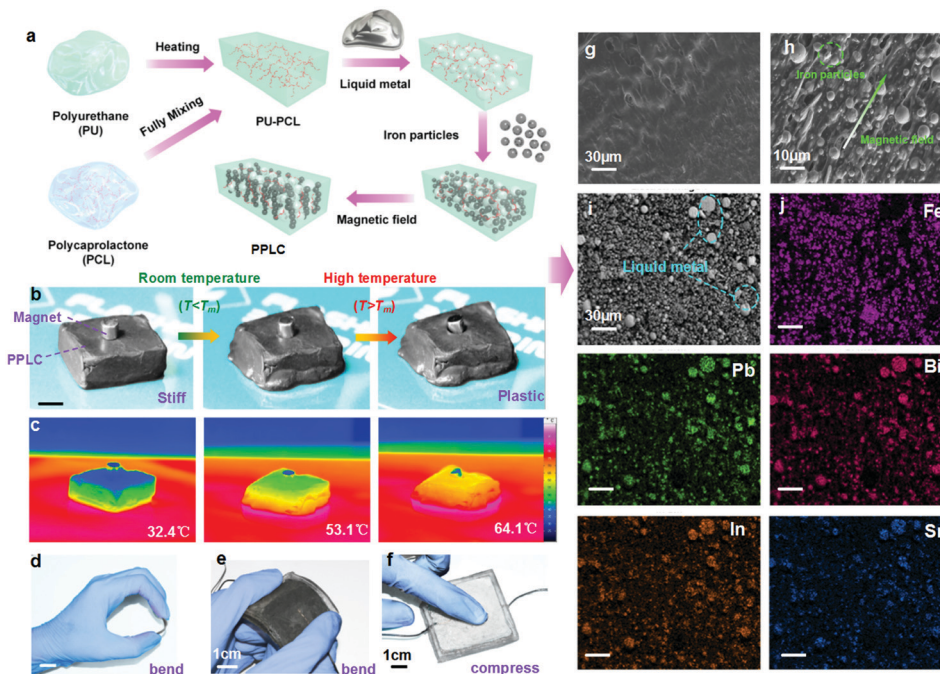*J. Mater. Chem. C*, 2021, **9**, 6568–6578 | **6569**

Fig. 1 (a) Fabrication processes of PPLC; (b) digital images and (c) thermal images of the PPLC heating by the platform of a 3D printer; digital images of the PPLC sensor under (d and e) bending and (f) compressing; scanning electron microscopy (SEM) images of (g) PU–PCL matrix, (h) PU–PCL–CI and (i) PPLC; and (j) the energy-dispersive X-ray spectroscopy (EDS) elemental mappings of PPLC.

were employed to test the magnetization and rheological properties of PPLC. A dynamic mechanical analyzer (DMA, ElectroForce 3200, TA instruments, Minnesota 55344 USA) was utilized to supply the compressive force. During the tests, the PPLC sensor was connected to the Modulab® material test system (Solartron analytical, AMETEK advanced measurement technology, Inc., United Kingdom) to evaluate the conductivity variation. In addition, a direct current (DC) power supply (ITECH IT6724), commercial electromagnetic coils, and permanent NdFeB magnet were employed to generate the magnetic field. A 3D printer (Flashforge, ltd, China) was employed to fabricate the molds.

Results and discussion

Rheological properties

Interestingly, the CIPs, HLM particles, and PCL crystals endowed PPLC with switchable mechanics. Here, the pure HLM droplet, PU–PCL, PU–PCL–LM, and PPLC samples with 20 mm diameter and 1 mm thickness were tested using a rheometer (Fig. 2a–c). The fluidity of the high-temperature liquid metal (HLM) at 60 °C is shown in Fig. S1 (ESI†); the viscosity of the HLM droplet gradually decreased with the shear rate from 10 s^{-1} to 40 s^{-1}. The shear strain oscillated at a frequency of 5 Hz with an amplitude of 0.1%. When the test temperature T increased from 5 °C to 80 °C, the storage modulus G' of the pure PU–PCL, PU–PCL–LM and PPLC dramatically decreased from 1.2 MPa, 3 MPa, and 3.3 MPa to 12 kPa, 14 kPa, and 22 kPa, respectively. The results clearly indicated the temperature-dependent properties of PPLC. What is more, the loss modulus G'' of PU–PCL–LM and PPLC gradually

increased with T when it was below 20 °C, but it kept decreasing for the pure matrix. It demonstrated that melting of HLM particles influenced the properties of PPLC. Therefore, the HLM particles could be effectively used as the temperature-controlling component in PPLC.

Afterward, the PPLC sensors with different CIP contents were tested by HyMDC to evaluate the magnetization properties. The saturation magnetization increased from 23.9 emu g^{-1} to 111.1 emu g^{-1} with the increase in the CIP content from 10 wt% to 50 wt% (Fig. 2d). It changed coincidently with the CIP content, which reflected the stable magnetization properties of CIPs. At the same time, the initial modulus G_0' of PPLC varied from 0.33 MPa to 0.67 MPa at 25 °C, proving the enhancement by CIPs. When T exceeded 60 °C, a dramatic drop of G' occurred, which indicated that the PCL crystal could be used as another temperature-controlling component (Fig. 2e and f). A similar variation tendency could be observed in G'' of PPLC. Therefore, the introduction of CIPs would not hinder the melting of temperature components (HLM and PCL). Moreover, the influence of the magnetic field was investigated. The PPLC sensor showed a typical magnetorheological (MR) effect (Fig. 2g–i). G' of 40 wt% PPLC increased from 0.13 MPa to 2.59 MPa as the magnetic flux density raised from 0 to 900 mT, with an MR effect of 1892%. After the HLM particles and PCL crystals were fully melted, the PPLC sensor was in a softened gel state, CIPs could overcome the binding of the matrix and aligned in chains along the magnetic field more easily. The saturated magneto-induced modulus also significantly increased with the CIP content, showing stronger magnetic interactions among iron particles. These results indicated that PPLC
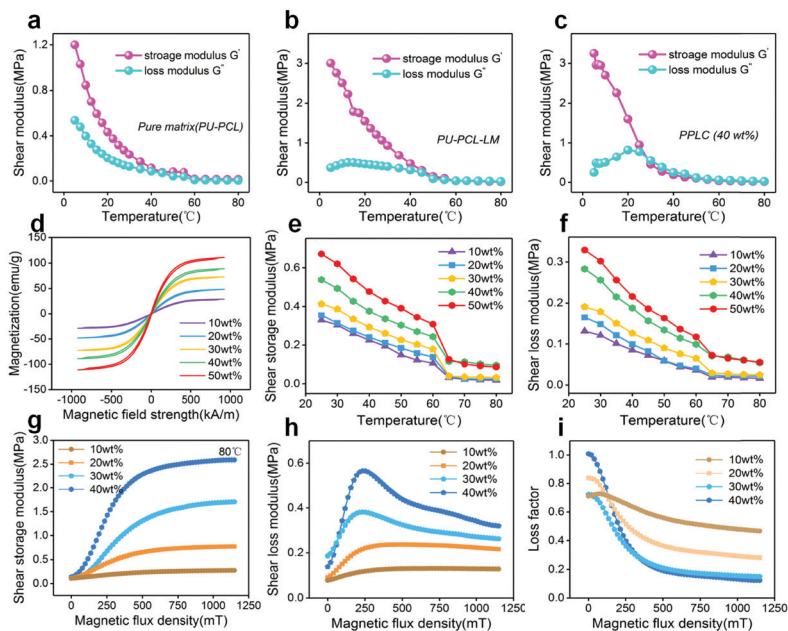
6570 | J. Mater. Chem. C, 2021, 9, 6568–6578

This journal is © The Royal Society of Chemistry 2021

Fig. 2   Temperature-dependent storage and loss modulus of (a) pure PU–PCL matrix, (b) PU–PCL–LM, and (c) PPLC; (d) the magnetization curves of PPLC with the CIP content from 10 wt% to 50 wt%, (e) storage and (f) loss modulus of PPLC with CIP content from 10 wt% to 50 wt% *versus* temperature; the (g) storage modulus, (h) loss modulus and (i) loss factor *versus* magnetic flux density.

could be employed in multifunctional flexible sensors due to the good magnetic field–temperature dependent properties.

Magnetic field sensing performance

Due to the magnetic interactions among the CIPs in the PU–PCL matrix (Fig. 1i), PPLC possessed good magnetic-induced properties. The interior structures of PPLC would deform and recover by the movement of CIPs, as the magnetic field was applied and removed. To systematically evaluate the mechanic–electric–magnetic-thermal properties, the sensing performance of PPLC sensor at different temperatures and magnetic fields was tested. Here, the sample with 20 mm diameter and 1 mm thickness was sandwiched between the copper foil and insulating layers and then placed between the plate rotor and electromagnetic base of the rheometer with 5 N preload (Fig. 3a). Two signal lines were employed to deliver the electrical signals from the sensor to the Modulab material test system.

First, the storage modulus G' and resistance R of the PPLC sensor with the CIP content from 10 wt% to 50 wt% were tested at 25 °C. The enhancement in CIPs on the mechanical properties has been illustrated in the previous part. Then, with the increase in CIP content from 10 wt% to 40 wt%, the R value significantly decreased from 119.6 MΩ to 2.9 MΩ, demonstrating the enhancement of conductivity (Fig. 3b). However, for 50 wt% PPLC sensors, excess CIPs would hinder the contacts among the HLM particles and reduce the effective conductive pathways, thus its conductivity was lower than that of the 40 wt% sample. Therefore, a 40 wt% PPLC sensor was chosen for the following sensing tests. With the increase in temperature T from 5 °C to 20 °C, the normal force F_N sharply decreased due to the softening of the PU–PCL matrix. Interestingly, the R value first increased

with T until 55 °C and then decreased with T (Fig. 3c). Because the HLM particles which contact copper foils were melted and fell into the soft matrix due to their high density at first, and the effective conductive pathways on the PPLC/copper foil interface were reduced, which led to an increase in R. When T was higher than 55 °C, the PCL crystals were melted. Therefore, the sample could not hold the shape under the compressing of the plate rotor. Then, the interface was squeezed and deformed, the contacts between HLM particles and copper foil layers were enhanced, which caused a decrease in R.

At room temperature (25 °C), the PPLC sensor was stiff enough to maintain the shape. By applying a triangle waveform cyclic magnetic field with an amplitude of 900 mT and a frequency of 0.016 Hz, the conductivity $\Delta\sigma$ ranged from 1.08 μS m^{-1} to 1.44 μS m^{-1} (Fig. 3d). The $\Delta\sigma$ gradually increased with the magnetic flux density. Because the magneto-interactions among CIPs were also enhanced by increasing the magnetic field. Thus, the magnetic force led to the deformation of the flexible PU–PCL matrix. Then, the HLM particles embedded in the matrix moved and the contacts among them gradually increased, and hence, $\Delta\sigma$ of the PPLC sensor changed dramatically. The magnetic piezo-conductivity coefficient PCC_m was calculated using the formula $(\Delta\sigma/\sigma_0)/B$, where σ_0 and $\Delta\sigma$ are the initial value and variation in conductivity, respectively, and B is the variation in magnetic flux density. The sensitivity of PPLC sensor was 0.376 ± 0.011 T^{-1} with the fit coefficient of 0.9966 (Fig. 3e). The $\Delta\sigma$ value linearly enhanced with the magnetic field, which demonstrated its feasibility in magnetic field sensing. Moreover, the impact of frequency on the sensing performance of the PPLC sensor was investigated (Fig. 3f). Keeping the amplitude at 900 mT, the $\Delta\sigma$ varied little under different frequencies
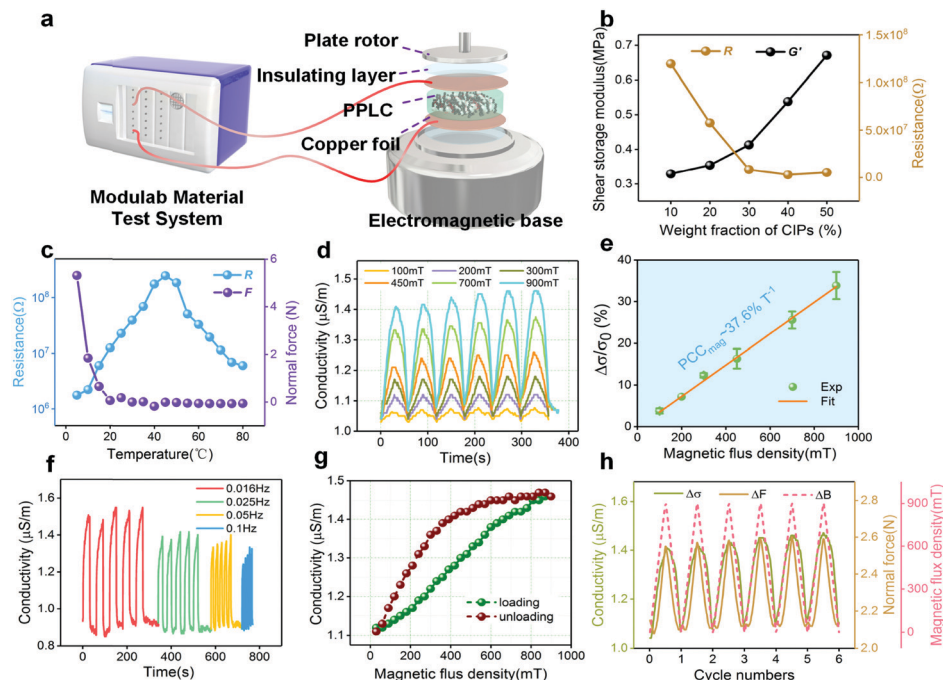
Fig. 3 (a) Schematic of the mechanical-electric-magnetic-thermal testing system; (b) storage modulus and resistance of the PPLC sensor *versus* CIP content; (c) normal force and resistance *versus* temperature. The room temperature (25 °C) magnetic field sensing tests: (d) the magnetic field dependent conductivityoof PPLC sensor; (e) $\Delta\sigma/\sigma_0$ *versus* magnetic flux density; (f) conductivity at different frequencies under an amplitude of 900 mT; (g) hysteresis loop of conductivity under a triangle waveform magnetic field at 25 °C; and (h) electrical and mechanical responses under a triangle waveform magnetic field.

(0.016 Hz, 0.025 Hz, 0.05 Hz, and 0.1 Hz), showing that the frequency of magnetic field hardly affected the sensing performance. Thanks to the stiff nature of the PPLC sensor at 25 °C, little hysteresis could be found during the loading and unloading phases under the amplitude of 900 mT (Fig. 3g). Furthermore, a triangle waveform cyclic magnetic field was employed to evaluate the responsive performance (Fig. 3h). The $\Delta\sigma$ and F_N values synchronously varied with the magnetic field, and the stable responsive performance further demonstrated its high potential in magneto-resistive strain sensors.

At high temperatures (60 °C), the melting of PCL crystals and HLM particles significantly influenced the properties of the PPLC sensor. By applying a square waveform cyclic magnetic field with an amplitude of 900 mT and a frequency of 0.016 Hz, the $\Delta\sigma$ and F_N values surprisingly heightened from 1.08 μS m^{-1} and 1.05 N to 1472 μS m^{-1} and 13.30 N, respectively (Fig. 4a and b). They could return to the initial state after the magnetic field was removed, showing the good repeatability. As T increased from 25 °C to 80 °C, $\Delta\sigma/\sigma_0$ and F_N gradually enhanced, especially over 60 °C (Fig. 4c). After being encapsulated in a PDMS shell, the $\Delta\sigma$ value of the PPLC sensor gradually increased under step compressing (Fig. 4d). By compressing the sample from 1 mm to 0.96 mm with an increment of 0.01 mm and a dwelling time of 30 s, $\Delta\sigma$ showed that the noise slightly affected the sensing performance. Due to the viscous nature of the PU–PCL matrix at 60 °C, the recovery of CIP chain structures in the unloading phase was hindered. Some hysteresis effects were found in the unloading phase of the triangle waveform

magnetic field. Moreover, the PPLC sensor could synchronously respond to the square waveform magnetic field in the loading and unloading phases, and $\Delta\sigma$ and F_N could quickly return to the initial state (Fig. 4e and f).

Here, we used a simplified mechanical and electrical model to calculate $\Delta\sigma$ of the PPLC sensor. A four-element model and a particle–particle tunnel current model were used to describe the viscoelastic behavior of the PU–PCL matrix and the tunneling effect among the CIPs[14,43] at 60 °C (Fig. 4g and h). According to the tunneling current model, when the gap between two particles was small enough, the electrons could overcome the binding of the matrix and across the gap, and then, the gap would be conductive, so that the two particles formed a conductive path as well as other particles, and the numerous conductive paths contributed to the conductivity of PPLC altogether. The four-element model was constructed by a spring, a dashpot and the Voigt-Kelvin model. The Voigt-Kelvin model contained a dashpot to show the viscosity η of cross-linked PU and another dashpot was added for the mixing viscosityη_1 of blended PU–PCL. When the stress of tunneling area $\sigma_v = kt$, the variation in the distance e between the two iron particles can be obtained using the following equation:

$$\delta e = e_0(\varepsilon_1 + \varepsilon_2 + \varepsilon_3) = e_0\left(\frac{\sigma_v t}{2\eta_1} + \frac{kt^2}{2G\tau} + \frac{\sigma_v}{E}\right)$$

$$= e_0\left(\frac{\sigma_v t}{2\eta_1} + \frac{kt^2}{2\eta} + \frac{\sigma_v}{E}\right) = e_0\left[\frac{k(\eta + \eta_1)t^2}{2\eta\eta_1} + \frac{\sigma_v}{E}\right]$$

(1)

6572 | *J. Mater. Chem. C*, 2021, **9**, 6568–6578
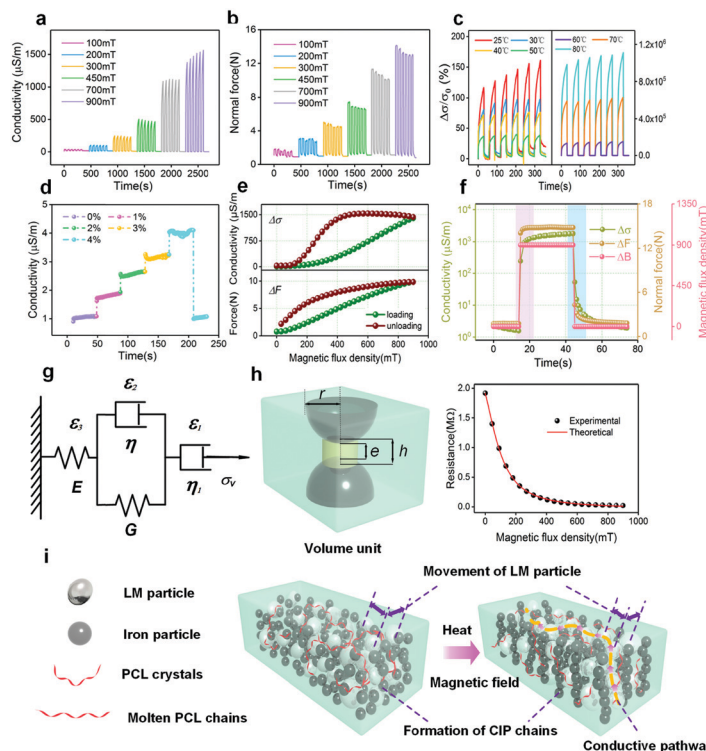
This journal is © The Royal Society of Chemistry 2021

Fig. 4 The high-temperature (60 °C) magnetic field sensing tests: the magnetic field-dependent (a) conductivityaand (b) normal force of the PPLC sensor; (c) $\Delta\sigma/\sigma_0$ versus magnetic flux density at different temperatures; (d) $\Delta\sigma$ under step loading with the increase in compressive strain; (e) hysteresis loop of conductivity and normal force under a triangle waveform magnetic field at 60 °C; (f) electrical and mechanical responses under a square waveform magnetic field; (g) a four-element model to represent the viscoelastic behavior; (h) schematic of the tunnel current model in the PPLC sensor and the comparison of results; and (i) schematic of the sensing mechanism.

Herein, $\tau = \dfrac{\eta}{G}$, which was far more than the testing time t. The resistance of the volume unit in the PPLC sensor was calculated as follows:

$$R_u = \rho\frac{e}{A} = \rho\frac{e}{\pi\left[r^2 - \left(r - \dfrac{h-e}{2}\right)^2\right]} = \rho_u\frac{2r + e}{A_u}$$

$$= \rho_u\frac{\phi(2r + e)^2}{\dfrac{4\pi r^3}{3}} \approx \rho_u\frac{3\phi}{\pi r} \tag{2}$$

Herein, ρ is the resistivity of the matrix, ρ_u is the average resistivity of PPLC, A_u is the area of volume unit, φ is the volume fraction of CIPs and r is the radius of particles, which was far more than the distance between particles e. We supposed that the CIPs were all in the same diameter and aligned in ideal line structures. By applying the magnetic field, the particles moved in the matrix, and the R_u varied

$$R_u = \rho\frac{e}{\pi\left[r^2 - \left(r - \dfrac{h-e}{2}\right)^2\right]} \approx \rho\frac{e}{\pi r(h-e)} = \rho\frac{e_0 - \delta e}{\pi r(h - e_0 + \delta e)} \tag{3}$$

Using eqn (1), we obtained

$$R_u = \rho\frac{e_0 - \delta e}{\pi r(h - e_0 + \delta e)} = \frac{\rho}{\pi r}\frac{1 - \dfrac{k(\eta + \eta_1)t^2}{2\eta\eta_1} + \dfrac{kt}{E}}{\dfrac{h - e_0}{e_0} + \dfrac{k(\eta + \eta_1)t^2}{2\eta\eta_1} + \dfrac{kt}{E}} \tag{4}$$

For the resistance of the whole sample, using eqn (2) and (4)

$$R_s = \rho_u\frac{H_S}{A_S} = \frac{\rho H_S\left[1 - \dfrac{k(\eta + \eta_1)t^2}{2\eta\eta_1} + \dfrac{kt}{E}\right]}{3\phi A_S\left[\dfrac{h - e_0}{e_0} + \dfrac{k(\eta + \eta_1)t^2}{2\eta\eta_1} + \dfrac{kt}{E}\right]} \tag{5}$$

For the tested samples, $H_S = 1.0$ mm, $A_S = 100\pi$ mm². Therefore, the magnetic field in the gap was uniform. The magnetic dipole force between two particles was calculated as follows:

$$F_d = -\frac{3\mu_0 m^2}{2\pi\mu_p r^5} \tag{6}$$

μ_p and m were the permeability and magnetic moment of particles. For the whole sample, the magnetic-induced normal force was calculated as follows:

$$F_N = \Sigma F_d = k_f B = k_f\beta t \tag{7}$$

Herein, k_f is a fitted parameter to show the relationship between the normal force and the magnetic flux density. During the test, the magnetic flux density linearly increased with a rate $\beta = 30$ mT s^{-1}.

Therefore, the stress of tunneling area can be obtained as follows:

$$\sigma_v = \frac{F_N}{A_S} \times \frac{A_u}{\pi r^2} = \frac{4F_N r}{3\phi A_S(2r+e)} \approx \frac{2k_f \beta t}{3\phi A_S} = kt \qquad (8)$$

Because the HLM particles were non-magnetic, the magnetic field could not directly influence the distribution of HLM particles. A parameter α_l was used to show the effect of HLM particles on the resistance. Using eqn (5) and (8), the relationship between the resistance of the sample and the magnetic flux density was obtained using the following equation:

$$
\begin{aligned}
R_s = \rho_u \frac{H_S}{A_S} &= \frac{\rho H_S \left[1 - \frac{k_f \beta(\eta+\eta_1)t^2}{3\phi A_S \eta\eta_1} + \frac{2k_f \beta t}{3\phi A_S E}\right]}{3\phi \alpha_l A_S \left[\frac{h-e_0}{e_0} + \frac{k_f \beta(\eta+\eta_1)t^2}{3\phi A_S \eta\eta_1} + \frac{2k_f \beta t}{3\phi A_S E}\right]} \\
&= \frac{\rho H_S \left[1 - \frac{k_f(\eta+\eta_1)}{3\phi A_S \eta\eta_1 \beta}B^2 + \frac{2k_f}{3\phi A_S E}B\right]}{3\phi \alpha_l A_S \left[\frac{h-e_0}{e_0} + \frac{k_f(\eta+\eta_1)}{3\phi A_S \eta\eta_1 \beta}B^2 + \frac{2k_f}{3\phi A_S E}B\right]}
\end{aligned}
\qquad (9)
$$

In eqn (9), the parameter ρ, η, η_1 and E were constant once confirmed. The comparison of the experimental and theoretical results is shown in Fig. 4h. The results matched well, with a fitting coefficient of 0.9991.

Moreover, the sensing mechanism of the PPLC sensor is illustrated in Fig. 4i. Initially, the HLM particles were dispersed in the CIP-doped PU–PCL matrix with few contacts. After a magnetic field was applied, the magnetic interactions among CIPs would lead to the deformation of the PU–PCL matrix and movement of HLM particles; thus, HLM particles would like to be in contact with their nearest neighbors, and then rupture the oxide layer and form percolating pathways. The higher the T, the softer the PU–PCL matrix, so the larger the deformation of matrix. HLM particles established contact with others more easily, showing higher $\Delta\sigma$. When T was higher than 60, the entangled PCL crystals inside the matrix totally melted into PCL chains, which led to a dramatic softening of the PPLC sensor (Fig. 1b and c, Movie S1, ESI†). Much more CIP chains were formed under the magnetic field without the hindrance of PCL crystals. During this process, numerous CIP chains squeezed the HLM particles and brought them in contact with others, thus additional effective conductive pathways were established, leading to a large enhancement of $\Delta\sigma$. The high magneto-sensitivity and good sensing performance further proved the feasibility in multifunctional composite sensors.

Compressive sensing performance

One of the most important features for flexible composite sensors was to maintain the electrical properties under the external stimuli like compressing. Therefore, the compressive sensing performance of the 40 wt% PPLC sensor was investigated at room temperature (25 °C). Here, a 3D-printed plastic cylinder (20 mm in diameter and 10 mm in thickness) was fixed on DMA to compress the PPLC sensor (20 mm in diameter and 1 mm in thickness) along thickness. The sample was also sandwiched by a copper foil and insulating layers, and connected to the Modulab material test system to record the signal.

By applying a triangle waveform cyclic compressing at a frequency of 0.1 Hz and an amplitude of 5%, $\Delta\sigma$ and compressive force F_c quickly increased from 1.08 μS m^{-1} and 1.25 N to 3.31 μS m^{-1} and 43.31 N, for which $\Delta\sigma/\sigma_0$ reached 212.4% (Fig. 5a, b and Fig. S1, ESI†). The electrical and mechanical performance of the PPLC sensor could fully recover in each compress-release cycle, demonstrating its good repeatability. When the amplitude increased from 2% to 8%, $\Delta\sigma$ also gradually increased. In particular, both the conductivity and force at the amplitude of 5% exhibited good stability and simultaneity (Fig. 5d and e). Herein, the piezo-conductivity coefficient PCC$_{com}$ is defined as $(\Delta\sigma/\sigma_0)/\varepsilon_c$ where ε_c is the compressive strain. It reached as high as 29.42 and 171.67 in pink (ε_c from 1% to 5%) and blue regions (ε_c from 5% to 8%), respectively (Fig. 5c). In the low ε_c region (pink), the PPLC sensor was slightly compressed by the 3D-printed cylinder and the deformation of the PU–PCL matrix was small, so the contacts among HLM particles gradually changed, leading to a slow increase in $\Delta\sigma$. As ε_c increased, the PPLC sensor was fully squeezed, and the gaps in the PU–PCL matrix significantly decreased. Thus, the contacts among HLM particles remarkably grew, showing higher $\Delta\sigma$.

Moreover, the loading waveform could be discriminated by the PPLC sensor. After applying cyclic sine, triangle, and square waveform compressing, $\Delta\sigma$ and ΔF_c showed the same variation tendency with ε_c, which further demonstrated the feasibility (Fig. 5f). As ε_c changed from 1% to 9% with the increment of 1%, $\Delta\sigma$ also increased step by step and remained stable during the dwelling time, which exhibited that noise hardly influenced the sensing performance (Fig. 5g). The responses of PPLC sensor were also barely impacted by frequency (Fig. 5h). Kept ε_c at 5%, $\Delta\sigma/\sigma_0$ slightly varied from 231% to 212% with the increase in frequency from 0.016 Hz to 0.1 Hz. Because the stability of the sensor was important, a stability test was conducted by compressing the PPLC sensor for 1000 cycles at a frequency of 0.1 Hz and an amplitude of 5% (Fig. 5i). The $\Delta\sigma$ only changed by 4.2%. The good compressive sensing performance further demonstrated that the PPLC sensor could be employed in multifunctional flexible strain sensors due to the good sensitivity and stability.

Shape memory property

The crystallization and melting of temperature-controlling components switched the properties of the PPLC sensor. The different melting points of PCL and HLM particles endowed the sensor with two reprogrammable temporary shapes. To investigate the shape memory property, PPLC was cut into a rod with the dimension of 50 mm × 2 mm × 1 mm and encapsulated in a PDMS shell with the dimension of 60 mm × 3 mm × 3 mm. At first, the rod was deformed into an "S" shape at a heating temperature (T_h) of 35 °C, and then fixed at a cooling

6574 | *J. Mater. Chem. C*, 2021, **9**, 6568–6578
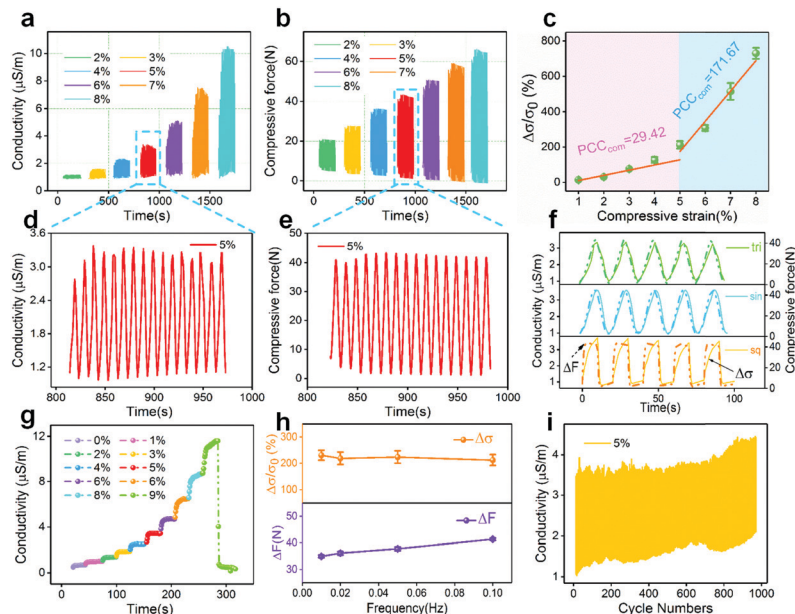
This journal is © The Royal Society of Chemistry 2021

Fig. 5 Compressive strain-dependent (a) conductivity and (b) force of the PPLC sensor; (c) $\Delta\sigma/\sigma_0$ versus compressive strain; typical (d) conductivity and (e) force under the compressive strain amplitude of 5%; (f) the electrical and mechanical responses under compressing with cyclic sine, triangle, and square waveform; (g) $\Delta\sigma$ under step loading with the increase in compressive strain; (h) conductivity and force versus compressive frequency under the compressive strain amplitude of 5%; (i) the stability under cyclic compressive loading.

temperature (T_c) of 0 °C. Taking the rod at room temperature (25 °C) again, the deformation could be partially recovered and the rod changed into a thinner "S" shape. However, after being deformed at T_h of 60 °C and fixed at T_c of 0 °C, the shape of rod would be unrecovered by taking it at 25 °C again. Thus, the rod could be transformed and locked into various shapes, for example, a "USTC" shape (Fig. 6a). In addition, all the locked shapes could be fully recovered by heating at 60 °C again, demonstrating the good shape memory property. Here, the melting point of bulk HLM was 47 °C in the experimental section. However, the melting and freezing points are size dependent and decrease as the diameter of the particles is

reduced due to the increased effect of surface energy in particles.[48] Thus, the melting point of HLM particles in the PPLC sensor slightly shifted to a lower value than pure HLM.

Moreover, the compressive tests were conducted using a rheometer to further present the shape memory effect. The sample was compressed using a plate rotor at different T_h (35 °C, 45 °C, and 55 °C) and fixed at 25 (Fig. 6c). Then, ε_c was unloaded and the sample was heated to T_h again. When T_h reached 55 °C, the shape of the sample was unrecovered, which further proved the stable shape memory property. A possible mechanism was proposed to describe the shape memory effect (Fig. 6d). When the rod was heated at 35 °C, the HLM particles
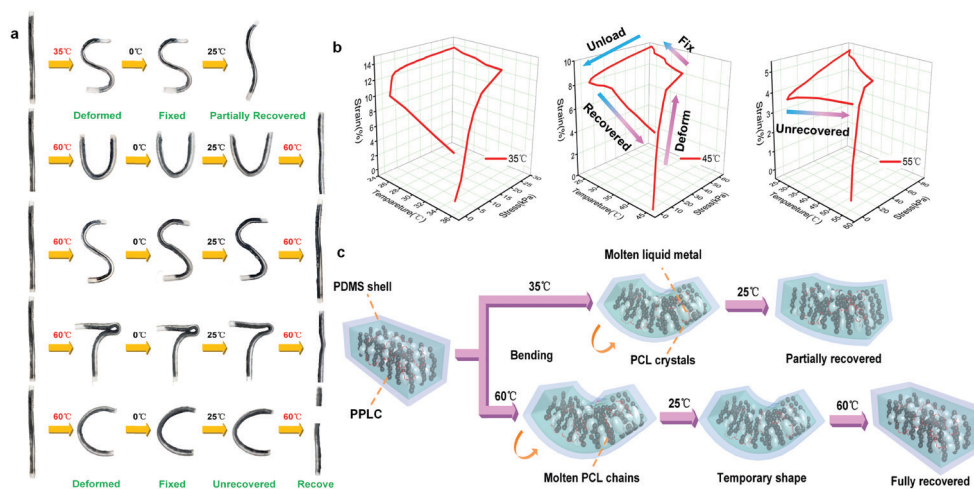

Fig. 6 (a) Digital images of the shape memory process; (b) a representative 3D plot for presenting shape memory properties of PPLC; and (c) schematic of the shape memory mechanism of PPLC.

This journal is © The Royal Society of Chemistry 2021

J. Mater. Chem. C, 2021, **9**, 6568–6578 | **6575**

were melted and they would move during the deformation process. However, entangled PCL crystals still existed in the matrix, which could hold the shape of whole rod. Then HLM particles were frozen at 0 °C with new distribution. During the deformation process, the PDMS has stored the elastic energy. After the rod was placed at 25 again, PDMS provided a driving force for the shape recovery, while the frozen HLM particles would maintain the temporary shape and hinder the shape recovery process. However, the HLM particles could not tolerate the driving force of PDMS, and therefore, the shape of the rod was partially recovered. When T_h was higher than 60 °C, both the HLM particles and entangled PCL crystals were totally melted. During the deformation and fixing process, the molten PCL chains moved inside the rod and then they were crystallized with new entangled structures. After cooling, the new entangled PCL crystals locked the shape of the rod, and thus the rod maintained the programmed temporary shape under the driving force of PDMS. Once the rod was heated to 60 °C again, the PCL crystals were melted and softened again; they could no longer tolerate the driving force of PDMS, and the shape of the rod fully recovered.

Applications of the PPLC sensor

The above-mentioned results revealed that the PPLC sensor possessed good sensing performance with triple-shape memory effects and magnetic field/compressive sensitivity, which proved it an ideal candidate for multifunctional flexible composite sensors. To further illustrate the applicability of the PPLC sensor, a smart alarm system was developed by integrating the PPLC sensor with breadboard, lighting emitting diode (LED), battery case and buzzer (Fig. 7a). Herein, the PPLC sensor and HLM plate with a dimension of 50 mm × 50 mm × 1 mm was encapsulated in a PDMS shell. A DC power was employed to apply current to the commercial electromagnetic coils for heat generation (Fig. 7b).

After applying a current of 4 A for 5 min, the temperature of coils reached 70 °C. Then, the DC power was turned off, the PPLC sensor was placed on the center of coils and a thermal camera was utilized to record the temperature variation during the monitoring process (Fig. 7c). T of the whole PPLC sensor quickly grew in seconds. Clear heat diffusion could be found on its cross-section. After monitoring for 120 s, the temperature gradient on the centerline of the PPLC sensor further proved its heat absorption capability (Fig. S4, ES11). After monitoring for 300 s, T of the top center point increased from 31.1 °C to 60.8 °C and remained stable, which indicated that all the PCL crystals and HLM particles inside the PPLC sensor were melted (Fig. 7d). Once the DC power was on and a current was applied to electromagnetic coils again, $\Delta\sigma$ significantly enhanced under the magnetic field or compressing (Fig. 7e), and then, the LED and buzzer would be triggered, shining and alarming sharply (Fig. 7b, Movie S2, ESI†). When the PPLC sensor was attached on a 3D printed wavy surface, it could fix on the surface and maintain its wavy shape by heating at 60 °C and then cooling at 25 °C (Fig. 7f). A self-adaptive sensing test based on the PPLC arm of soft PPLC grippers was conducted to show the combination of these two functions (Fig. S5, ESI†). After heating at 80 °C for 5 min, the PPLC arm could detect the 3D-printed wavy surface, memory the shape and, then, fully fix on it. The conductivity synchronously varied with the attaching process of the PPLC arm. Thanks to the multiple sensing ability, the PPLC sensor was demonstrated for the feasibility in multifunctional flexible composite sensors.

The soft grippers can be constructed by using the PPLC sensor due to their ability of adapting morphology while grabbing objects. In general, the untethered control and reversible actuation in lifting, holding and releasing objects were the mostly desired capabilities for soft grippers. Taking PPLC's advantage of magnetically driven and shape memory properties,
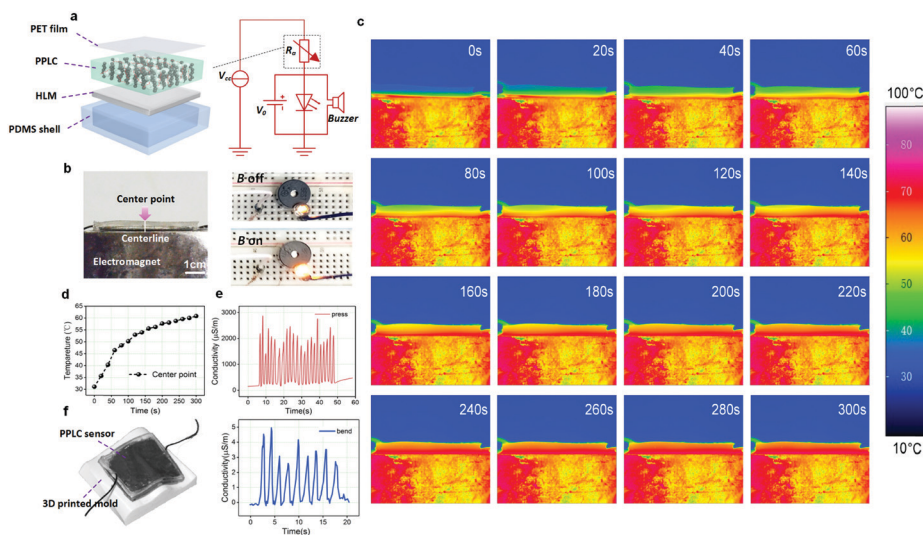

Fig. 7 (a) Schematic and circuit diagram of the smart alarm device; (b) digital images of the smart alarm device with the magnetic field off and on; (c) thermal images of the PPLC sensor during the real-time monitoring process and corresponding (d) temperature and (e) conductivity variation; and (f) digital images of the PPLC sensor on a wavy surface and corresponding conductivity variation.
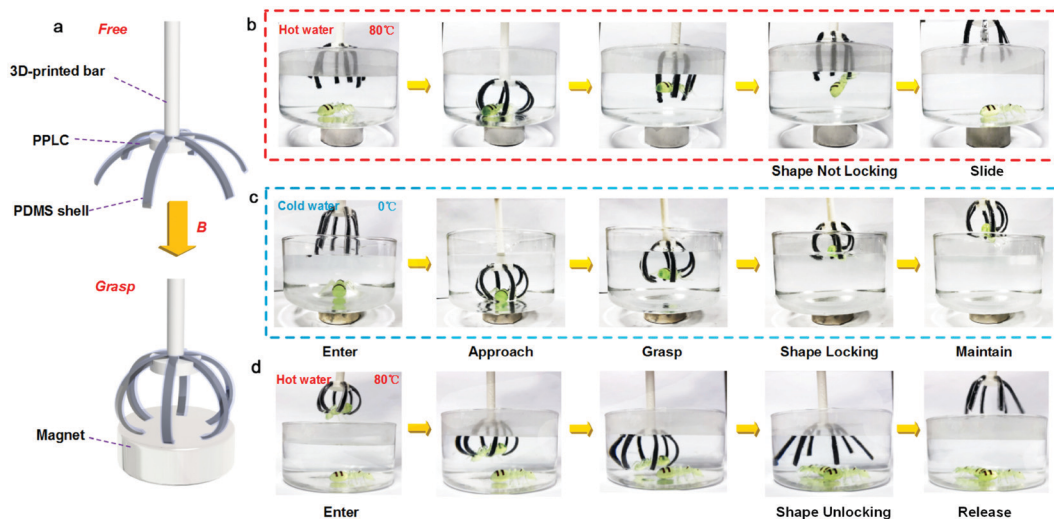
Fig. 8 (a) Schematic of a six-arm PPLC gripper; (b) PPLC gripper lifting a spider toy (b) without and (c) with shape locking; and (d) PPLC gripper releasing a spider toy with shape unlocking.

we demonstrated a PPLC-based soft robotic gripper that could autonomously grab and release objects. Fig. 8a shows the design of a six-arm PPLC gripper. By immersing in hot water (80 °C), the grippers softened and grasped the spider toy by attracting the magnet under the bottom (Fig. 8b). At this moment, the spider toy slipped during the lifting process of the gripper due to the decrease in magnetic field. However, as demonstrated in Fig. 8c, the gripper could be stiffened and locked into an actuated shape after immersion in cold water (0 °C). Then, the spider toy could be easily lifted without external magnetic field. Besides, the shape-locked gripper could autonomously release the spider toy after immersion in hot water again. Therefore, the fast and switchable actuating of the PPLC gripper permitted the potential in multiple use and grasping motions for objects with complex morphology, which further broadened the application.

Conclusions

In summary, we have fabricated a magneto-resistive flexible strain sensor with multiple sensitivity, triple-shape memory effect, and magnetically driven property. Two types of temperature-controlling components (PCL and HLM) and one type of magnetic particles (CIPs) were utilized for achieving the triple-shape memory effect and multiple sensing. The PPLC sensor could effectively respond to an external magnetic field, compressive strain and heat for the sensing and actuating operations in functions such as a smart alarm and smart gripper. With recent rapid development for the fabrication of multifunctional flexible composite sensors, these results indicated that the PPLC sensor could serve as a platform for various applications such as biomedical devices, reconfigurable flexible electronics, e-skins, and autonomous soft robotics.

CRediT authorship contribution statement

Tao Hu: Investigation, Formal analysis, Validation, Writing – original draft, Methodology, Visualization, Writing – review &

editing. Shouhu Xuan: Conceptualization, Writing – review & editing. Quan Shu: Writing – review & editing. Zhenbang Xu: Visualization, Methodology. Longjiang Shen: Formal analysis. Jun Li: Visualization, Methodology. Xinglong Gong: Resources, Supervision, Project administration, Funding acquisition.

Conflicts of interest

There are no conflicts to declare.

Acknowledgements

References

1 D. H. Kim and J. A. Rogers, *Adv. Mater.*, 2008, **20**, 4887–4892.
2 C. S. Boland, U. Khan, G. Ryan, S. Barwich, R. Charifou, A. Harvey, C. Backes, Z. Li, M. S. Ferreira, M. E. Mobius, R. J. Young and J. N. Coleman, *Science*, 2016, **354**, 1257–1260.
3 S. He, C. X. Zhou, H. L. Chen, X. L. Liu, H. Li, W. M. Ma, X. Su and T. Han, *J. Mater. Chem. C*, 2020, **8**, 3553–3561.
4 K. Takei, T. Takahashi, J. C. Ho, H. Ko, A. G. Gillies, P. W. Leu, R. S. Fearing and A. Javey, *Nat. Mater.*, 2010, **9**, 821–826.
5 T. Sekitani, H. Nakajima, H. Maeda, T. Fukushima, T. Aida, K. Hata and T. Someya, *Nat. Mater.*, 2009, **8**, 494–499.
6 Y. Q. Liu, K. He, G. Chen, W. R. Leow and X. D. Chen, *Chem. Rev.*, 2017, **117**, 12893–12941.

This journal is © The Royal Society of Chemistry 2021

J. Mater. Chem. C, 2021, **9**, 6568–6578 | **6577**

7 D. B. Chen, Q. P. Liu, Z. W. Han, J. Q. Zhang, H. L. Song, K. J. Wang, Z. Y. Song, S. F. Wen, Y. Zhou, C. Z. Yan and Y. S. Shi, *Adv. Sci.*, 2020, **7**, 2000584.

8 N. Festin, C. Plesse, P. Pirim, C. Chevrot and F. Vidal, *Sens. Actuators, B*, 2014, **193**, 82–88.

9 Y. H. Wu, R. M. Zhen, H. Z. Liu, S. Q. Liu, Z. F. Deng, P. P. Wang, S. Chen and L. Liu, *J. Mater. Chem. C*, 2017, **5**, 12483–12491.

10 L. Shi, Z. Li, M. Chen, Y. J. Qin, Y. Z. Jiang and L. M. Wu, *Nat. Commun.*, 2020, **11**, 3529.

11 G. Lee, G. Y. Bae, J. H. Son, S. Lee, S. W. Kim, D. Kim, S. G. Lee and K. Cho, *Adv. Sci.*, 2020, **7**, 2001184.

12 P. Bahoumina, H. Hallil, J. L. Lachaud, A. Abdelghani, K. Frigui, S. Bila, D. Baillargeat, A. Ravichandran, P. Coquet, C. Paraguad, E. Pichonatd, H. Happy, D. Rebiere and C. Dejous, *Sens. Actuators, B*, 2017, **249**, 708–714.

13 W. J. Huang, K. Dai, Y. Zhai, H. Liu, P. F. Zhan, J. C. Gao, G. Q. Zheng, C. T. Liu and C. Y. Shen, *ACS Appl. Mater. Interfaces*, 2017, **9**, 42266–42277.

14 L. H. Wang and L. H. Cheng, *Carbon*, 2014, **71**, 319–331.

15 P. Puneetha, S. P. R. Mallem, Y. W. Lee and J. Shim, *ACS Appl. Mater. Interfaces*, 2020, **12**, 36660–36669.

16 Y. Y. Lu, K. C. Xu, L. S. Zhang, M. Deguchi, H. Shishido, T. Arie, R. H. Pan, A. Hayashi, L. Shen, S. Akita and K. Takei, *ACS Nano*, 2020, **14**, 10966–10975.

17 M. G. Saborio, S. X. Cai, J. B. Tang, M. B. Ghasemian, M. Mayyas, J. L. Han, M. J. Christoe, S. H. Peng, P. Koshy, D. Esrafilzadeh, R. Jalili, C. H. Wang and K. Kalantar-Zadeh, *Small*, 2020, **16**, 1903753.

18 S. H. Shin, D. H. Park, J. Y. Jung, M. H. Lee and J. Nah, *ACS Appl. Mater. Interfaces*, 2017, **9**, 9233–9238.

19 M. Amjadi, A. Pichitpajongkit, S. Lee, S. Ryu and I. Park, *ACS Nano*, 2014, **8**, 5154–5163.

20 M. D. Dickey, *Adv. Mater.*, 2017, **29**, 1606425.

21 A. Fassler and C. Majidi, *Adv. Mater.*, 2015, **27**, 1928–1932.

22 E. J. Markvicka, M. D. Bartlett, X. N. Huang and C. Majidi, *Nat. Mater.*, 2018, **17**, 618–624.

23 G. L. Yun, S. Y. Tang, S. S. Sun, D. Yuan, Q. B. Zhao, L. Deng, S. Yan, H. P. Du, M. D. Dickey and W. H. Li, *Nat. Commun.*, 2019, **10**, 1300.

24 G. L. Yun, S. Y. Tang, Q. B. Zhao, Y. X. Zhang, H. D. Lu, D. Yuan, S. S. Sun, L. Deng, M. D. Dickey and W. H. Li, *Matter*, 2020, **3**, 824–841.

25 Y. Lou, H. Z. Liu and J. Y. Zhang, *Chem. Eng. J.*, 2020, **399**, 125732.

26 M. J. Ford, D. K. Patel, C. F. Pan, S. Bergbreiter and C. Majidi, *Adv. Mater.*, 2020, **32**, 2002929.

27 Y. M. Xin, H. Peng, J. Xu and J. Y. Zhang, *Adv. Funct. Mater.*, 2019, **29**, 1808989.

28 D. Kim, Y. Lee, D. W. Lee, W. Choi, K. Yoo and J. B. Lee, *Sens. Actuators, B*, 2015, **207**, 199–205.

29 S. Merhebi, M. Mayyas, R. Abbasi, M. J. Christoe, J. L. Han, J. B. Tang, M. A. Rahim, J. Yang, T. T. Tan, D. W. Chu, J. Zhang, S. A. Li, C. H. Wang, K. Kalantar-Zadeh and F. M. Allioux, *ACS Appl. Mater. Interfaces*, 2020, **12**, 20119–20128.

30 R. Guo, X. Y. Sun, B. Yuan, H. Z. Wang and J. Liu, *Adv. Sci.*, 2019, **6**, 1901478.

31 D. H. Yu, Y. Liao, Y. C. Song, S. L. Wang, H. Y. Wan, Y. H. Zeng, T. Yin, W. H. Yang and Z. Z. He, *Adv. Sci.*, 2020, **7**, 2000177.

32 T. Hu, S. H. Xuan, L. Ding and X. L. Gong, *Sens. Actuators, B*, 2020, **314**, 128095.

33 L. F. Zhu, Y. Z. Chen, W. H. Shang, S. Handschuh-Wang, X. H. Zhou, T. S. Gan, Q. X. Wu, Y. Z. Liu and X. C. Zhou, *J. Mater. Chem. C*, 2019, **7**, 10166–10172.

34 S. Q. Liang, Y. Y. Li, Y. Z. Chen, J. B. Yang, T. P. Zhu, D. Y. Zhu, C. X. He, Y. Z. Liu, S. Handschuh-Wang and X. C. Zhou, *J. Mater. Chem. C*, 2017, **5**, 1586–1590.

35 Q. Zhao, H. J. Qi and T. Xie, *Prog. Polym. Sci.*, 2015, **49-50**, 79–120.

36 A. Lendlein and O. E. C. Gould, *Nat. Rev. Mater.*, 2019, **4**, 116–133.

37 Q. J. Ze, X. Kuang, S. Wu, J. Wong, S. M. Montgomery, R. D. Zhang, J. M. Kovitz, F. Y. Yang, H. J. Qi and R. K. Zhao, *Adv. Mater.*, 2020, **32**, 1906657.

38 X. H. Xu, P. D. Fan, J. Ren, Y. Cheng, J. K. Ren, J. Zhao and R. Song, *Compos. Sci. Technol.*, 2018, **168**, 255–262.

39 U. N. Kumar, K. Kratz, M. Heuchel, M. Behl and A. Lendlein, *Adv. Mater.*, 2011, **23**, 4157–4162.

40 S. Qi, J. Fu, Y. P. Xie, Y. P. Li, R. Y. Gan and M. Yu, *Compos. Sci. Technol.*, 2019, **183**, 107817.

41 T. Hu, S. H. Xuan, L. Ding and X. L. Gong, *Mater. Des.*, 2018, **156**, 528–537.

42 L. Ding, L. Pei, S. H. Xuan, X. W. Fan, X. F. Cao, Y. Wang and X. L. Gong, *Adv. Electron. Mater.*, 2020, **6**, 1900653.

43 H. M. Pang, S. H. Xuan, T. X. Liu and X. L. Gong, *Soft Matter*, 2015, **11**, 6893–6902.

44 Y. Alapan, A. C. Karacakol, S. N. Guzelhan, I. Isik and M. Sitti, *Sci. Adv.*, 2020, **6**, eabc6414.

45 Y. Kim, H. Yuk, R. K. Zhao, S. A. Chester and X. H. Zhao, *Nature*, 2018, **558**, 274–279.

46 W. Q. Hu, G. Z. Lum, M. Mastrangeli and M. Sitti, *Nature*, 2018, **554**, 81–85.

47 S. Qi, H. Y. Guo, J. Fu, Y. P. Xie, M. Zhu and M. Yu, *Compos. Sci. Technol.*, 2020, **188**, 107973.

48 M. H. Malakooti, N. Kazem, J. J. Yan, C. F. Pan, E. J. Markvicka, K. Matyjaszewski and C. Majidi, *Adv. Funct. Mater.*, 2019, **29**, 1906098.

6578 | *J. Mater. Chem. C*, 2021, **9**, 6568–6578

This journal is © The Royal Society of Chemistry 2021